Urban Flood Mapping with Bi-temporal Multispectral Imagery via a Self-supervised Learning Framework

Bo Peng, Qunying Huang, Jamp Vongkusolkit, Song Gao, Daniel B. Wright, Zheng N. Fang, Yi Qiang

Abstract-Near realtime ood mapping in densely-populated urban areas is critical for emergency response. The strong heterogeneity of urban areas poses a big challenge for accurate near realtime ood mapping. However, previous studies on automatic methods for urban ood mapping perform infeasible in near realtime or fail to generalize well to other oods, for several reasons. First, multi-temporal pixel-wise ood mapping requires accurate image registration, hindering the efficiency of large-scale processing. Although automatic image registration has been investigated, precisely co-registered multi-temporal image sequence requires time-consuming fine tuning. Additionally, the oods may lead to the loss of many corresponding image points across multitemporal images for accurate co-registration. Second, existing unsupervised methods generally rely on hand-crafted features for oodwater detection. Such features may not well represent the patterns of oodwaters in different areas due to inconsistent weather conditions, illumination, and oodwater spectra. This study proposes a self-supervised learning framework for patch-wise urban ood mapping using bi-temporal multispectral satellite imagery. Patch-wise change vector analysis is used with patch features learned through a self-supervised autoencoder to produce patch-wise change maps showing potentially oodaffected areas. Post-processing including spectral and spatial filtering is applied to these patch-wise change maps to remove non- ood related changes. Final ood maps and parameter sensitivities were evaluated using several performance metrics. Two ood events from areas with differing degrees of urbanization were considered: Hurricane Harvey ood (2017) in Houston, Texas and Hurricane Florence ood (2018) in Lumberton, North Carolina. The proposed method shows strong performance for self-supervised urban ood mapping.

Index Terms—Urban, ood mapping, multispectral imagery, self-supervised learning

I. INTRODUCTION

Manuscript received xxx; revised xxx. This work was supported by the National Science Foundation under Grant #1940091, the Vilas Associates Competition Award, Microsoft AI for Earth Grant, and the Trewartha Graduate Research Award from Department of Geography at University of Wisconsin-Madison.

- B. Peng is with the Department of Geography, Department of Electrical and Computer Engineering, University of Wisconsin Madison, Madison, WI 53706, USA. (e-mail: bo.peng@wisc.edu).
- Q. Huang, J. Vongkusolkit, and S. Gao are with the Department of Geography, University of Wisconsin Madison, Madison, WI 53706, USA. (e-mail: qhuang46@wisc.edu; vongkusolkit@wisc.edu; song.gao@wisc.edu)
- D. B. Wright is with the Department of Civil and Environmental Engineering, University of Wisconsin Madison, Madison, WI 53706, USA. (e-mail: danielb.wright@wisc.edu)
- Z. N. Fang is with the Department of Civil Engineering, University of Texas, Arlington, Arlington, TX 76019, USA. (e-mail: nickfang@uta.edu)
- Y. Qiang is with the School of Geosciences, University of South Florida, Tampa, FL 33620, USA. (e-mail: qiangy@usf.edu)

THROUGHOUT the history of human civilization, floods have brought catastrophe to human settlements, including huge losses of life and property. As the most frequent natural disaster, floods account for more than 75% of federally-declared disasters in the U.S. [1]. Records of flood events globally show that the number of individuals affected by floods is growing at an alarming rate [2]. In response, the United Nations (UN) has set the goal to rapidly and accurately respond to upcoming floods for protecting vulnerable people and mitigating economic losses, as stated in the UN Sustainable Development Goal 11 (2015–2030) [3]. To help meet this goal, improved methods for realtime flood extent mapping over dense urban regions to support flood response efforts are needed.

Remote sensing (RS) data have played an important role in large-scale flood extent mapping. Optical multispectral (MS) or hyperspectral (HS) satellite imagery in particular has unique advantages for identifying flooded areas by virtue of the abundant spectral information associated with floodwater [4]-[9]. Wieland et al. [7] developed an operational processing chain for flood extent mapping with Landsat and Sentinel-2 images. Wang et al. [6] used MS imargery from Landsat 8 to explore the role of normalized difference water index (NDWI) in super-resolution flood inundation mapping. Li et al. [4] proposed to use discrete particle swarm optimization for sub-pixel flood mapping on Landsat images. Recently, Du et al. [10] and Tong et al. [11] proposed improved particle swarm optimization methods for endmember extraction, which have great potential for sub-pixel flood mapping. These aforementioned flood mapping studies, however, have focused on rural areas with relatively homogeneous image backgrounds. Meanwhile, flood extent mapping is insufficiently investigated in urban areas due to heterogeneous land cover and land use, low spatial resolution of MS imagery, and lack of flood extent ground truth datasets [12], [13].

Satellite sensors are capable of scanning the entire earth surface with a high revisit frequency, abundant spectral bands, and high spatial resolution, which enable high-resolution mapping over heterogeneous urban areas. There have been a growing number of satellite constellations in orbit, including PlanetLab's [14] PlanetScope, RapidEye, and SkySat and Maxar/DigitalGlobe's [15] QuickBird, WorldView, IKONOS, and GeoEye. The raw pixel digital numbers in multi-temporal optical imagery are usually inconsistent for the same land cover types due to the changing weather and illumination conditions [16]. Such inconsistency is a barrier to robust

floodwater detection from multi-temporal RS images using data-driven machine learning models. Geometric and radiometric corrections are needed before surface reflectance imagery products can be useful for consistent spectral-based identification of flooded areas [12], [13].

Regarding the mapping strategy, both pixel-wise [4], [5], [16]–[20] and patch-wise [12], [13], [21] models have been proposed for flood mapping. Pixel-wise flood mapping methods assign each pixel of the input imagery a label (e.g., flooded or non-flooded) whereas patch-wise methods predict the class of an entire patch cropped from the imagery. Both pixel- and patch-wise mapping have been explored for flood extent mapping, since each has unique advantages in specific scenarios. Patch-wise mapping has been widely used for flood mapping over heterogeneous urban areas [12], [13], [21], for several reasons. First, patch-wise mapping helps mitigate the impact of errors from multi-temporal image registration. It is challenging to have large-scale co-registered multi-temporal high spatial resolution images in near realtime due to radiometric and geometric distortions [22]-[24]. Intensive labor work is required to fine-tune the corresponding image points for accurate co-registration. Such pre-processing is time-consuming for large-scale flood mapping, precluding application in near realtime. Moreover, since floodwaters may have covered a large part of the study area, many corresponding image points across the multi-temporal images may not be available for image registration. Second, pixel-wise mapping requires pixelwise human annotations for model training and validation, which is more time-consuming and labor-intensive than patchwise mapping. Even if un-/self-supervised methods are used, human annotated validation data are still required for model evaluation over a small study area, which is expensive due to the heterogeneous image background over urban areas. For example, to map flooded areas on an image of size 100 100 pixels (px), pixel-wise labeling requires 10⁴ labels whereas patch-wise labeling requires only 10^2 labels if the image is divided into non-overlapping patches of size 10 10 px. In addition, it is more difficult to accurately label a pixel than a patch for heterogeneous urban areas.

It is worth noting that, for urban flood mapping with high spatial resolution imagery, the U.S. Federal Emergency Management Agency (FEMA) defined the National Flood Mapping Products [25] with flooded areas that are either submerged or surrounded by floodwaters. As such, not only floodwater pixels but also their neighboring non-floodwater pixels (e.g., building pixels surrounded by floodwaters) are included in flooded areas. When combined with self-supervised learning, patchwise mapping is able to address the aforementioned issues associated with pixel-wise mapping and to produce large-scale flood maps in near realtime. The patch-wise flood maps are consistent with FEMA's Flood Mapping Products since non-floodwater pixels near floodwater pixels within the same patch are included in flooded areas.

To our best knowledge, few studies have investigated self-/un-supervised patch-based methods using optical MS imagery for flood mapping over heterogeneous urban areas. To overcome the above limitations, this study proposes a self-supervised patch-based urban flood mapping method using bi-

temporal pre- and post-flood MS satellite imagery with four spectral bands including blue (B), green (G), red (R), and near infrared (NIR). Self-supervised learning is a special type of unsupervised learning [26], [27]. Self-supervised models are trained with automatically generated labels, which require no manual annotation for training. In this study, patch features were learned in a self-supervised manner using an autoencoder model [28]. We performed bi-temporal patch change vector analysis followed by spectral and spatial filtering to map urban floods in near realtime. The method was evaluated for two hurricane-induced flood events in the United States: Hurricane Harvey (2017) in Houston, Texas, and Hurricane Florence (2018) in Lumberton, North Carolina. Results show that the method provides strong performance and robust generalizability.

Major contributions of this study include:

- The proposed method obviates massive human-annotated training data through a self-supervised learning framework. This enables the application of the method in large-scale and realtime, which offers the potential for its deployment in operational workflows at the front lines of emergency humanitarian assistance and disaster relief.
- The flood maps generated by the proposed method for the two study areas demonstrate the method's robustness and generalizability in emergency response for upcoming floods.
- The proposed method is resilient to non-flood related changes between the bi-temporal data by leveraging spectral and spatial filtering, which effectively removed nonflood related changes for accurate flood mapping.
- Although this framework is proposed to map urban floods in near realtime, it also paves the way for damage mapping in response to other types of disasters such as wildfires, earthquakes, etc.

The structure of the paper is organized as follows. Related work is discussed in Section II. The study areas and datasets are described in Section III. The proposed method is presented in Section IV. Experimental results are summarized in Section V. Discussion about the results is given in Section VI. Finally, Section VII concludes major outcomes of this study and the future work.

II. RELATED WORK

Recent studies have shown promising results of supervised patch-based land cover mapping and its potential in flood mapping. Li *et al.* [21] developed an active self-learning convolutional neural network (CNN) to classify the synthetic-aperture-radar (SAR) image patches into three classes (i.e., non-flooded, flooded with buildings, and flooded without buildings). Peng *et al.* [12], [13] designed a Siamese CNN model to evaluate the patch similarity for identification of flooded MS image patches. Song *et al.* [29] and Sharma *et al.* [30] proposed CNN-based models to map land cover with superior performance compared with pixel-based methods, especially in heterogeneous urban areas.

The aforementioned CNN based models demonstrate the power of data-driven supervised deep learning and computer

vision in flood mapping by leveraging an increasing volume of RS data with massive human labels. However, such a time-consuming manual labeling process poses further challenges for near realtime flood mapping and emergency response in a large scale. Additionally, these models often fail to generalize well when applied to other floods or locations [12], [16], [27].

To address the challenges associated with supervised methods, unsupervised pixel-wise flood mapping with bi-temporal pre- and post-flood imagery has been explored with as few human annotations as possible through change detection [24], [31]-[34] followed by automatic thresholding techniques such as the minimum error thresholding proposed by Kittler and Illingworth (KI) [35], [36] and Otsu's method [37], [38]. In 2009-2010, the IEEE Geoscience and Remote Sensing Society launched a Data Fusion Contest [34] for flood mapping based on multi-temporal change detection, which involves both supervised and unsupervised flood mapping on optical MS and SAR data. In the category of unsupervised flood mapping with optical MS data, the winning algorithm [34] used the near infrared (NIR) band of pre- and post-flood imagery with an unsupervised clustering algorithm, leveraging the high absorption of water in the NIR band. Byun et al. [24] proposed an unsupervised change detection approach to pixel-wise flood mapping based on bi-temporal MS image fusion with detection of spectral distortion. Schlaffer et al. [32] conducted harmonic analysis of multi-temporal SAR imagery to identify flooded pixels, which showed strong deviations from the corresponding non-flooded pixels. Giustarini et al. [33] developed a hybrid framework integrating SAR backscatter thresholding, flooded region growing, and change detection for flood mapping using bi-temporal SAR imagery. Du et al. [39] recently proposed the unsupervised deep slow feature analysis for unsupervised pixel-wise change detection based on bi-temporal MS imagery, which can be further applied in flood mapping.

The previous works discussed above showed good results of flood mapping in an unsupervised manner without intensive human labeling of training data. Unfortunately, those unsupervised methods focused on pixel-wise mapping, which are not directly applicable to patch-wise mapping over heterogeneous urban areas.

To sum up, patch-wise flood mapping over heterogeneous urban areas using a self-supervised deep learning approach is still missing in previous works to the best of the authors' knowledge, which is the main objective of this study.

III. STUDY AREA AND DATA SETS

This work investigates self-supervised mapping of urban floods in two different cities in the United States (U.S.), including the 2017 Hurricane Harvey flood in Houston, Texas (Fig. 1), and the 2018 Hurricane Florence flood in Lumberton, North Carolina (Fig. 2). We choose these two study areas because both floods involve dense residential, industrial, and commercial areas. Experiments based on these two study areas will validate the effectiveness of the proposed method in flood mapping over heterogeneous urban areas.

For each flood event, the data used in this study were bitemporal pre- and post-flood MS imagery from PlanetLab [14]

 $\label{thm:constraints} TABLE\ I$ Specifications for Harvey and Florence multispectral images.

Specifications	Harvey	Florence	
Hurricane Landfall Date	August 25, 2017	September 14, 2018	
Image Date (Before)	July 31, 2017	August 31, 2018	
Image Date (After)	August 31, 2017	September 18, 2018	
Spectral Band	B, G, R, NIR		
Height, Width (px)	(1850, 3070)	(2240, 2940)	
Spatial Resolution (m)		3	
Pre-processing	Surface Reflectance		
Total # of Patches	56,795	65,856	
Ratio of FL	0.1777	0.1916	

covering the same geographic area. All images are surface reflectance products with four spectral bands (i.e., B, G, R, and NIR). Spatial resolution of both data sets over the two study areas are 3 meters (m) of ground sampling distance.

This work performed patch-wise flood extent mapping, where non-overlapping corresponding pre- and post-flood patches were cropped from the before and after bi-temporal MS images, respectively. Each patch is of size 10 10 px and thus covers ground area of 30 30 m. The goal of this study is to classify the post-flood patches into flooded (FL) or non-flooded (NF).

Although the proposed method is self-supervised (i.e., without human annotated training labels), ground truth data is needed for quantitative evaluation of experimental results. This ground truth data were generated by manually labeling the data sets for the two study areas. All post-flood image patches were labeled by visual inspection of the very high resolution (VHR) imagery with spatial resolution of 0.3 m from National Oceanic and Atmospheric Administration (NOAA) collected on the same day as those from PlanetLab. We cropped patches from NOAA's VHR imagery, with each patch covering the same geographical area (i.e., 30 m 30 m) as the co-located PlanetLab MS patch. Each NOAA VHR patch thus contains 100 px 100 px (100 = 30/0.3), which was labeled by three expert annotators based on the flooded area within the patch. The ground truth label of each post-flood patch was determined by the majority vote out of all three annotations. Patches with a tiny negligible flooded area or with floodwaters under tree canopy were intentionally labeled as NF [12], [21]. 56,795 labeled patches (10,094 FL and 46,701 NF) were collected for the Harvey data set and 65,856 labeled patches (12,619 FL and 53,237 NF) were collected for the Florence data set. More detailed specifications of the data sets are summarized in Table I.

IV. METHODOLOGY

A. Problem Formulation

Given a pair of pre- and post-flood MS images $(\mathbf{I}^{pre}, \mathbf{I}^{post})$, we cropped M rows by N columns non-overlapping patch pairs $(\mathbf{I}^{pre}_{i,j}, \mathbf{I}^{post}_{i,j})$, where $i=1,2,\ldots,M$ and $j=1,2,\ldots,N$ are patch coordinates. Each patch is with 10-10 px and 4 bands. This study proposed a fully self-supervised framework \mathcal{F} for generating the flood map \mathbf{P} by

$$\mathbf{P} = \mathcal{F}(\mathbf{I}^{pre}, \mathbf{I}^{post})
= \mathcal{F}_4(\mathcal{F}_3(\mathcal{F}_2(\mathcal{F}_1(\mathbf{I}^{pre}, \mathbf{I}^{post}))))$$
(1)

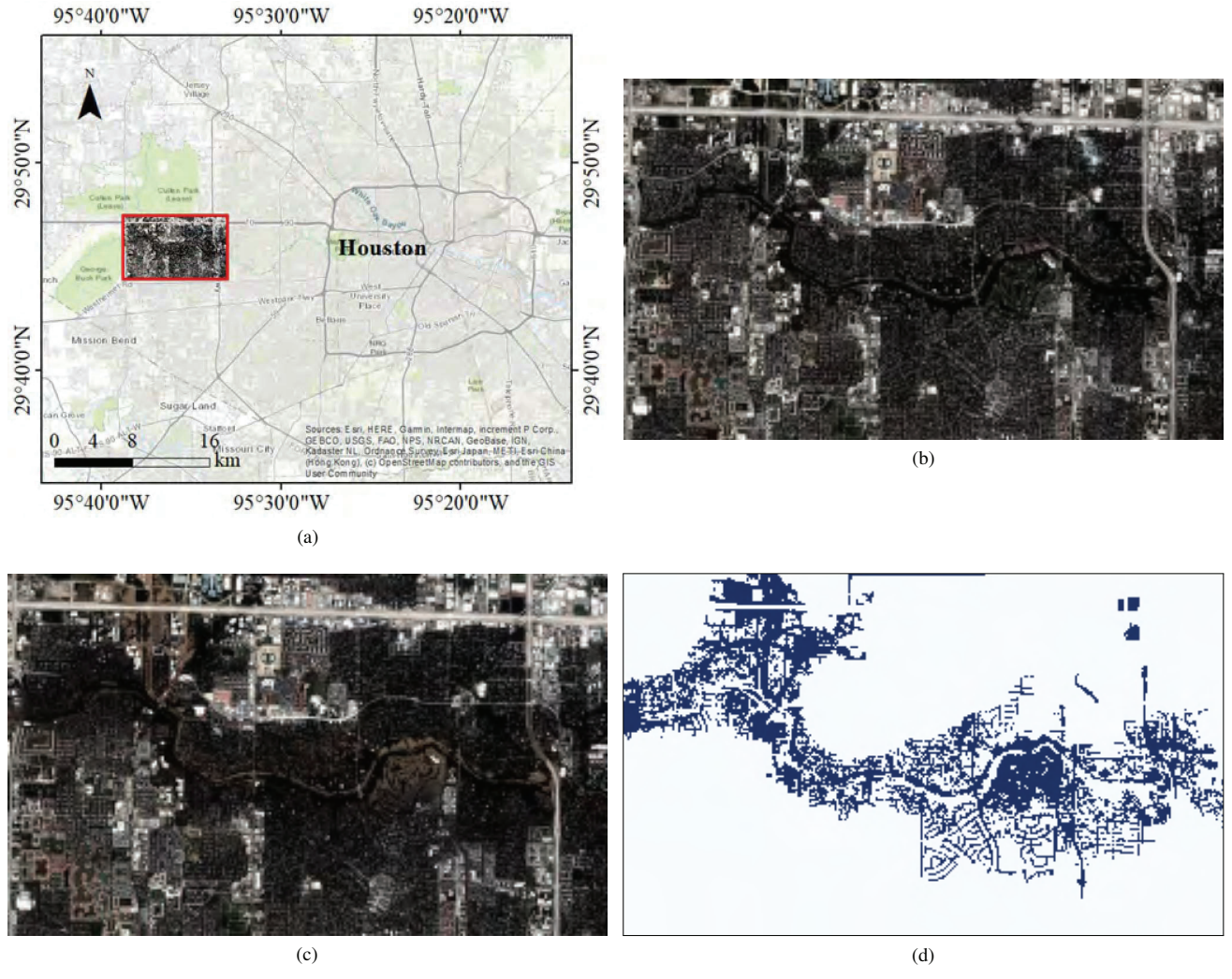


Fig. 1. Harvey data. (a) Study area of Harvey flood; (b) Satellite image before flood; (c) Satellite image after flood; (d) Manually-classified ground truth of patch-wise flood extent map.

where $(\mathcal{F}_1, \mathcal{F}_2, \mathcal{F}_3, \mathcal{F}_4)$ denote the four interlocking modules in the framework \mathcal{F} , including (1) \mathcal{F}_1 : patch encoding for patch feature extraction, (2) \mathcal{F}_2 : patch change vector analysis for *initial* flood mapping, (3) \mathcal{F}_3 : spectral filtering to remove non-flooded changes for *intermediate* flood mapping, and (4) \mathcal{F}_4 : spatial filtering to remove noise for *final* flood mapping. Fig. 3a illustrates the workflow of the proposed framework.

Since the pre- and post-flood images were captured with a time interval of less than one month, we assume that the land cover changes over the study areas mainly resulted from floods. Accordingly, patch similarity estimation based on patch feature vectors was used for patch change detection and *initial* flood mapping. The more similar $(\mathbf{I}_{i,j}^{pre}, \mathbf{I}_{i,j}^{post})$, the less likely that $\mathbf{I}_{i,j}^{post}$ was indeed flooded.

Furthermore, *initial* flood maps based on patch change detection may lead to unexpected false alarms due to noise and isolated non-flooded changes. Using the spectral signature of floodwaters and the spatial topology of flooded areas, we conducted further spectral filtering to remove non-flooded changes and spatial filtering to remove minor isolated or noisy

changes for accurate flooded patch detection.

B. Patch Encoding

The **Patch Encoding** module learned the multidimensional features of both pre- and post-flood patches $(\mathbf{I}_{i,j}^{pre}, \mathbf{I}_{i,j}^{post})$, for patch change detection. Specifically, each pair of $(\mathbf{I}_{i,j}^{pre}, \mathbf{I}_{i,j}^{post})$ were fed into a pre-trained Siamese patch *Encoder* to extract the representative features $(\mathbf{c}_{i,j}^{pre}, \mathbf{c}_{i,j}^{post})$. Patch change detection was then conducted in the **Patch Change Vector Analysis** module based on the encoded patch features $(\mathbf{c}_{i,j}^{pre}, \mathbf{c}_{i,j}^{post})$.

To enable self-supervised learning of patch features without human annotated labels, we developed an autoencoder model, which encodes the high-dimensional input into low-dimensional features and then decodes the features for reconstructing the input. As such, the autoencoder model was trained with patches as both the input and the target. The *Encoder* of the pre-trained autoencoder was then used for encoding the patches. The network architecture of the autoencoder developed in this study is shown in Fig. 3b with hyperparameters listed in Table II, which includes *Encoder* and

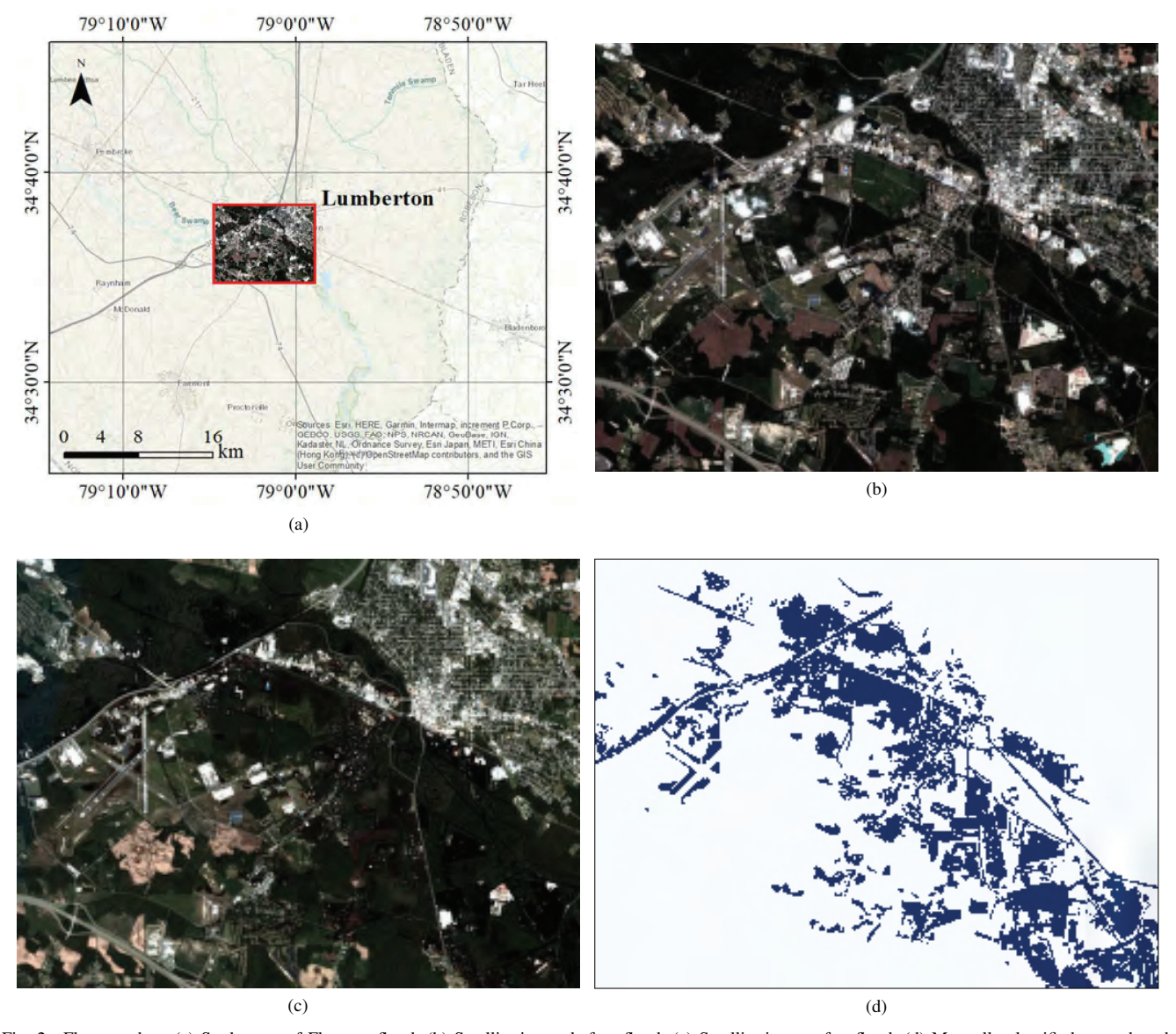


Fig. 2. Florence data. (a) Study area of Florence flood; (b) Satellite image before flood; (c) Satellite image after flood; (d) Manually-classified ground truth of patch-wise flood extent map.

Decoder sub-networks. The *Encoder* consists of several layers of convolutional nets (Conv) while the *Decoder* is composed of a stack of transposed convolutional nets (ConvTrans).

We trained the Siamese autoencoder for the pre- and post-flood patches with shared weights for further patch change detection. 80% pairs of pre- and post-flood patches were used for training, and the rest 20% for validation. We took batches of bi-temporal patch pairs $(\mathbf{I}_{i,j}^{pre}, \mathbf{I}_{i,j}^{post})$ as both inputs and targets of the autoencoder, using the Adam optimizer [40] along with the L1 loss, $\mathcal{L}(x,y)$, defined in Eq. 2.

$$\mathcal{L}(x,y) = \frac{1}{B} \int_{1}^{B} x_i - y_i$$
 (2)

where x and y denote the output and target of the model, and B is the number of patches in each batch. In the autoencoder model, the target is the input itself. It should be noted that the class imbalance (i.e. the relative frequencies of FL and

NF patches) of the data sets (Table I) does not undermine the performance of patch change detection for FL patch detection. This is a major advantage of self-supervised patch change detection for flood mapping compared to supervised models trained with highly imbalanced data sets, in which class weights typically must be set during training [12], [21].

We start with the learning rate of 0.01 and reduce it by a factor of 10 if the validation loss does not decrease for 10 consecutive epochs. Default momentum parameters $(\beta_1,\beta_2)=(0.9,0.999)$ of the Adam optimizer were used. Weight decay was set to 1e-5. For better model generalization, common data augmentations were used, including random rotation with degrees in $[0^\circ,90^\circ,180^\circ,270^\circ]$, random vertical and horizontal flipping, and normalization to the range of [0,1]. After training with 150 epochs, the pre-trained *Encoder* was then used to encode both pre- and post-flood patches for further patch change detection.

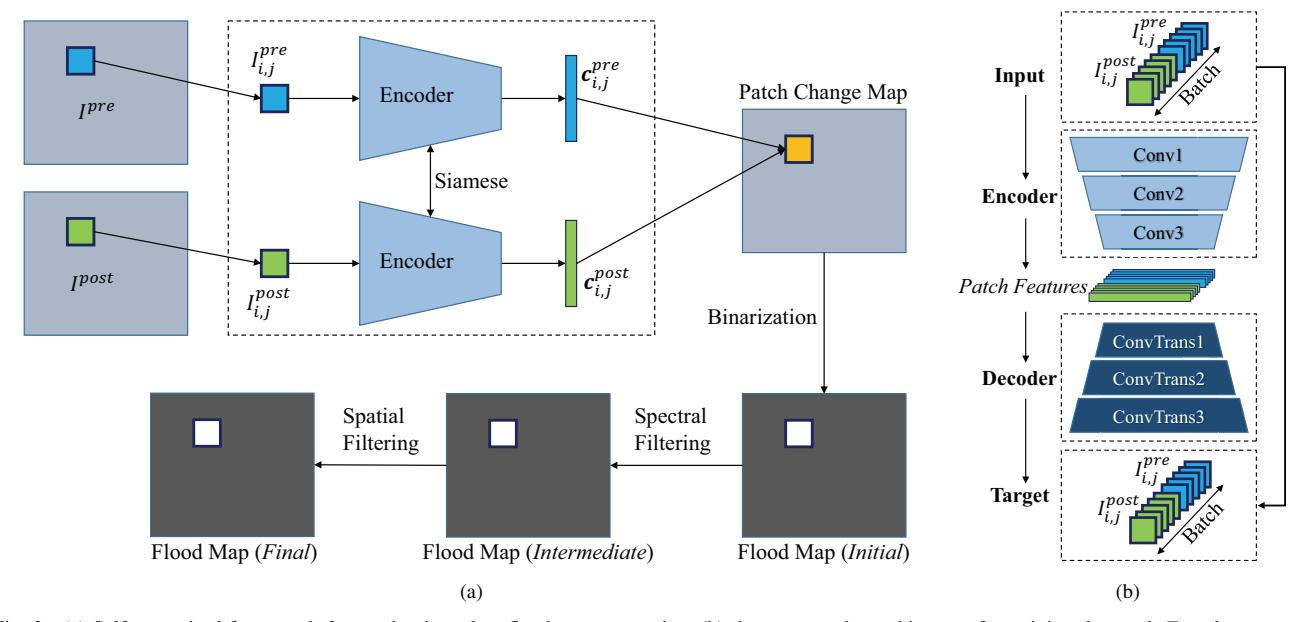


Fig. 3. (a) Self-supervised framework for patch-wise urban flood extent mapping, (b) the autoencoder architecture for training the patch Encoder.

TABLE II
AUTOENCODER HYPERPARAMETERS

Module	Operation	Parameters
Input	Image Patches	Size: [Batch, 4, 10, 10]
Encoder Conv2		Convolution (out: 64, kernel: 3) Batch Normalization LeakyReLU (0.01) Max-pool (2)
		Convolution (out: 128, kernel: 3) Batch Normalization LeakyReLU (0.01) Max-pool (2)
	Conv3	Convolution (out: 64, kernel: 1) Sigmoid
Decoder	ConvTrans1	ConvTransposed (out: 128, kernerl: 1) Batch Normalization LeakyReLU (0.01) Upsample (scale: 2, bilinear)
	ConvTrans2	ConvTransposed (out: 64, kernerl: 3) Batch Normalization LeakyReLU (0.01) Upsample (scale: 2, bilinear)
	ConvTrans3	ConvTransposed (out: 4, kernerl: 3) Sigmoid
Target	Same as Input	Size: [Batch, 4, 10, 10]

C. Patch Change Vector Analysis

The **Patch Change Vector Analysis** (**Patch-CVA**) module followed the widely used technique of change vector analysis (CVA) [41]–[44] to select potential FL patches. We computed the magnitude and direction of change between pairs of preand post-flood patch features $(\mathbf{c}_{i,j}^{pre}, \mathbf{c}_{i,j}^{post})$. The magnitude component of the change is defined as the Euclidean distance (ED) between the $\mathbf{c}_{i,j}^{pre}$ and $\mathbf{c}_{i,j}^{post}$ (Eq. 3).

$$\mathrm{ED}\left(\mathbf{c}_{i,j}^{pre},\mathbf{c}_{i,j}^{post} \ = \ \mathbf{c}_{i,j}^{pre} - \mathbf{c}_{i,j}^{post} \ _{2} \right. \tag{3}$$

Suppose the patch feature vector consists of K elements, traditional direction change was defined as $\alpha = (\alpha_1, \alpha_2, \dots, \alpha_k, \dots, \alpha_K)$ where α_k is computed by Eq. 4.

$$\cos\left(\alpha_{k}\right) = \frac{\mathbf{c}_{i,j}^{pre}(k) - \mathbf{c}_{i,j}^{post}(k)}{\mathrm{ED}\left(\mathbf{c}_{i,p}^{pre}, \mathbf{c}_{i,j}^{post}\right)} \tag{4}$$

where $\mathbf{c}_{i,j}^{pre}(k)$ and $\mathbf{c}_{i,j}^{post}(k)$ denote the k^{th} elements in $\mathbf{c}_{i,j}^{pre}$ and $\mathbf{c}_{i,j}^{post}$, respectively.

However, the above direction change in traditional CVA is not often used [43] because the direction component in traditional CVA often leads to a quantity α with the same dimension as the input change vectors and even more complex high-dimensional change maps for further change detection. Hence, we used the cosine similarity score (Eq. 5) to measure the angle between the pre- and post-flood patch feature vectors, which indicated the direction component of the change.

$$\cos \mathbf{c}_{i,j}^{pre}, \mathbf{c}_{i,j}^{post} = \frac{\left(\mathbf{c}_{i,j}^{pre} \ ^{\top} \left(\mathbf{c}_{i,j}^{post} \right) \right)}{\mathbf{c}_{i,j}^{pre} \mathbf{c}_{i,j}^{post} \mathbf{c}_{i,j}^{post}}$$
(5)

where $\cos \mathbf{c}_{i,j}^{pre}, \mathbf{c}_{i,j}^{post}$ denotes the cosine score of the angle between $\mathbf{c}_{i,j}^{pre}$ and $\mathbf{c}_{i,j}^{post}$.

Following the maps of magnitude and direction changes, binarization through automatic thresholding was used to select initial potential FL patches. We applied the technique proposed by Rosin [45], [46] to select the threshold, where the *corner* of the histogram was selected as the threshold. Rosin [45], [46] assumed that the histogram of the change map of either magnitude or direction is a unimodal distribution with one dominant population with respect to the secondary population. Specifically, the selected point on the histogram corresponding to the threshold is the most distant from the line between the peak and the end of the histogram (Fig. 4).

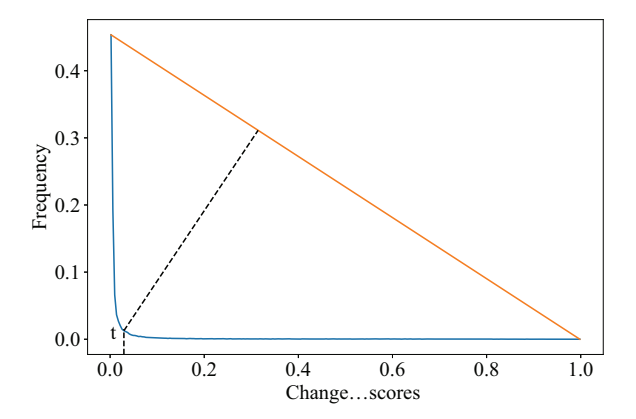


Fig. 4. Rosin's method [45], [46] for selection of the threshold t based on the histogram of the magnitude or direction change map.

Based on the above thresholding technique, we binarized both magnitude and direction change maps to obtain the *initial* flood maps.

D. Spectral Filtering

The *initial* flood maps may contain multiple types of changes not related to floodwaters—shadows, human built-up areas, errors in radiometric or geometric corrections, etc. Since all FL post-flood patches contain floodwater pixels, spectral features of the *initial* flood maps were investigated to remove non-flood related changes.

Floodwater typically has lower surface reflectance than that of other major land cover types such as built-up areas and vegetation. We performed a pixel-wise binary unsupervised clustering for all pixels in potential post-flood FL patches based on the *initial* flood maps. In this study, k-means [47] clustering on raw pixel spectra was used for both Harvey and Florence data sets. It should be noted that the spectra of some buildings in dense neighborhoods are very similar to those of floodwaters (Fig. 5), leading to misclassification of some building pixels. By leveraging Microsoft building footprints [48], we removed building pixels classified as FL and thus obtained *intermediate* flood maps.

E. Spatial Filtering

After **Spectral Filtering**, there can still exist false alarms in the *intermediate* flood map due to small isolated areas previously identified as FL patches due to noise, shadow, and other errors. Often, these areas are isolated and far from major flooded areas. The spatial topology of flood movement means that that flooded patches tend to be close to each other. Therefore, we assume that FL patches are connected in major flooded areas. FL patches need not be strictly adjacent to each other in heterogeneous urban areas, however, since patches with floodwaters under trees are defined as NF [12], [21], leading to disconnection of some FL patches. Therefore, we defined in this study that FL patches were connected if they were within a pre-defined maximum distance of d patches as illustrated in Fig. 6.

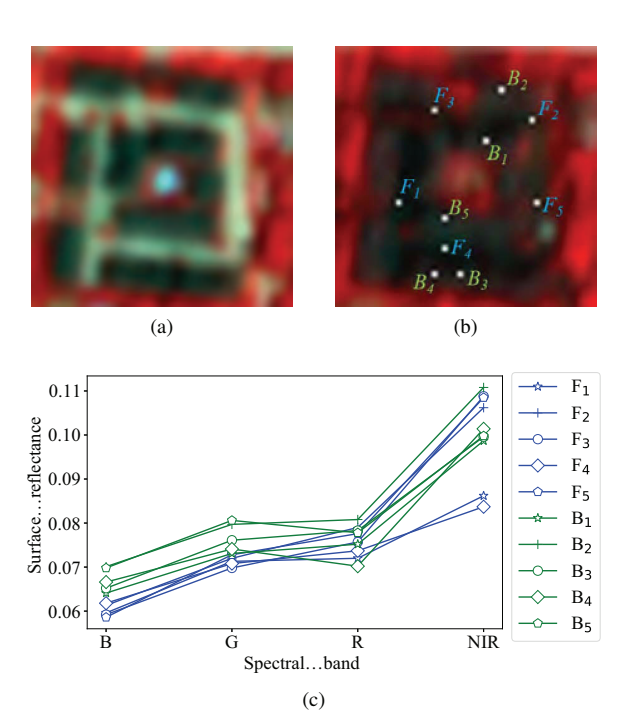


Fig. 5. Buildings and floodwaters in dense neighborhoods show similar spectral features. (a) a false-color image of a neighborhood before flood. (b) the corresponding image after flood. (c) the spectral plots of five building samples (B_1, B_2, \ldots, B_5) and five floodwater samples (F_1, F_2, \ldots, F_5) .

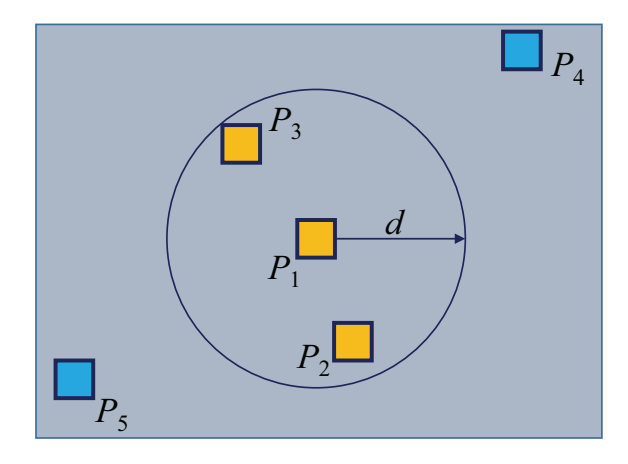


Fig. 6. Patch connectivity: patches (P_1, P_2, P_3) marked in yellow are connected since they are within a distance of d patches whereas patches (P_4, P_5) marked in blue are not connected to any patches in the map since they are far away from other patches.

After identification of major flooded areas through connectivity analysis, small isolated areas were removed if they contained less than a pre-defined minimum number of *a* patches in the *intermediate* flood maps as they exhibited false alarms. Finally, the *final* flood maps were generated based on both *direction* and *magnitude* change, respectively.

F. Performance Evaluation

This work investigated the problem of flooded patch detection. With ground truth labels, we computed the number of true positives (TPs), false positives (FPs), true negatives

TABLE III
TIME CONSUMPTION ON TRAINING THE AUTOENCODERS AND ENCODING
ALL IMAGE PATCHES WITH THE PRE-TRAINED ENCODERS FOR HARVEY
AND FLORENCE DATASETS.

Dataset	Training (mins)	Encoding (mins)
Harvey	40.97	0.33
Florence	46.76	0.37

(TNs), and false negatives (FNs), respectively. Therefore, we quantitatively evaluated the performance of the proposed framework using precision (Pr), recall (Re), F1 score, and overall accuracy (OA), defined as

$$Pr = \frac{TPs}{TPs + FPs}$$

$$Re = \frac{TPs}{TPs + FNs}$$

$$F1 = \frac{2}{1/Pr + 1/Re}$$

$$OA = \frac{TPs + TNs}{TPs + FPs + TNs + FNs}$$
(6)

Additionally, as the proposed framework generated the flood maps, we also evaluated the accuracy based on the intersection over union (IoU), also known as the Jaccard Index [49]. Given the ground truth flood map ${\bf G}$ and the predicted map ${\bf P}$, IoU is defined as

$$IoU(\mathbf{G}, \mathbf{P}) = \frac{\text{Area of Intersection of } (\mathbf{G}, \mathbf{P})}{\text{Area of Union of } (\mathbf{G}, \mathbf{P})} = \frac{\mathbf{G} \quad \mathbf{P}}{\mathbf{G} \quad \mathbf{P}}$$

V. EXPERIMENTAL RESULTS

This section describes the application of the proposed method for patch-wise urban flood mapping over two study areas in the U.S., including 1) the 2017 Hurricane Harvey Flood at Houston, Texas and 2) the 2018 Hurricane Florence Flood at Lumberton, North Carolina. The **Patch Encoding** models in Section IV-B were trained on a server with 64-bit Ubuntu 16.04.6 LTS and a 24 GiB Titan RTX GPU based on PyTorch [50]. Table III lists the time consumption on training the autoencoders for 150 epochs and encoding all the preand post-flood image patches with the pre-trained encoders for both Harvey and Florence datasets, respectively.

All other experiments were conducted on a Dell workstation with an Intel(R) Xeon(R) W-2125 CPU @ 4.00 GHz 8, 16 GiB RAM, and 64-bit Window 10.

A. Flood Event 1: Harvey

1) Results of Patch-CVA: Using the pre-trained encoder described in Section IV-B, we encoded both pre- and post-flood patches into low-dimensional feature vectors. Fig. 7 shows the patch-wise change maps generated based on the changes of direction (Fig. 7a) and magnitude (Fig. 7c), respectively. Both change maps were normalized into the range of [0, 1].

By leveraging Rosin's thresholding technique discussed in Section IV-C, we selected the thresholds of both direction

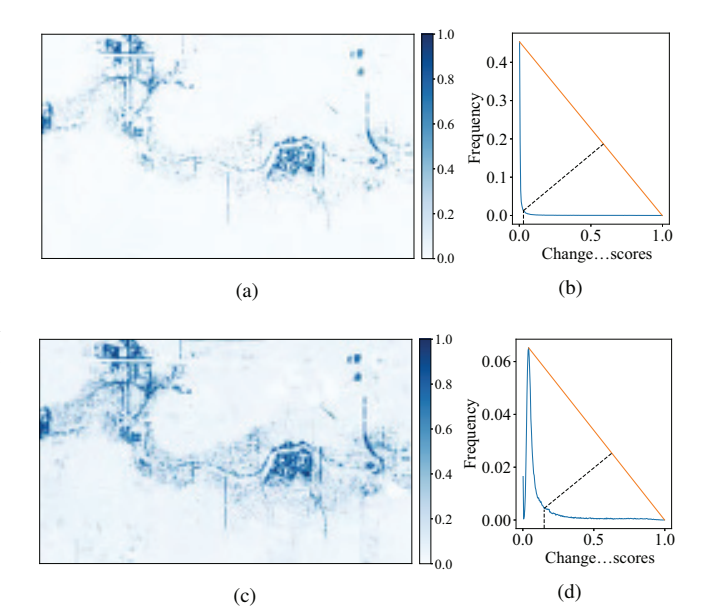


Fig. 7. Harvey change maps based on encoded pre- and post-flood patch features: (a) *direction* change map and (b) histogram with Rosin's thresholding corresponding to *direction* change; (c) *magnitude* change map and (d) histogram with Rosin's thresholding corresponding to *magnitude* change.

TABLE IV HARVEY: QUANTITATIVE RESULTS OF THE PATCH-WISE FLOOD MAPS AT DIFFERENT PROCESSING STAGES BASED ON THE CHANGE OF direction and magnitude (DIR: DIRECTION; MAG: MAGNITUDE; INT: INITIAL; IMD: INTERMEDIATE: FNL: FINAL)

Type	Stage	Pr	Re	F1	IoU	OA
	(a) INT	0.8939	0.9175	0.9055	0.8274	0.9659
DIR	(b) IMD	0.9205	0.9133	0.9169	0.8465	0.9705
	(c) FNL	0.9428	0.9130	0.9276	0.8651	0.9747
	(a) INT	0.8579	0.9313	0.8931	0.8068	0.9603
MAG	(b) IME	0.8874	0.9278	0.9071	0.8301	0.9662
	(c) FNL	0.9107	0.9276	0.9190	0.8502	0.9709

and magnitude change maps based on their corresponding histograms (Figs. 7b and 7d).

We thus obtained two different binary classification maps (Fig. 8a and 9a) associated with the *direction* and *magnitude* change maps, respectively. Compared with ground truth labels in Fig. 1d, we highlighted TPs in blue, FPs in red, and FNs in yellow. Corresponding to Figs. 8a and 9a, we evaluated the Pr, Re, F1, IoU, and OA of the *initial* flood maps as listed in Table IV, where the best results were marked in bold.

We also tested binarization of the initial *direction* change map (Fig. 7a) using the thresholding methods proposed by Otsu [38] and Kittler and Illingworth (KI) [35]. Table V summarizes the results associated with each thresholding method. Rosin's method outperformed Otsu's and KI's methods in terms of F1, IoU, and OA. Otsu's method produced high Pr with very low Re whereas KI's method performed conversely with low Pr but high Re. Only Rosin's method was able to consistently perform well in all metrics.

2) Results of spectral filtering: We clustered pixels located in patches detected in the above initial binary change

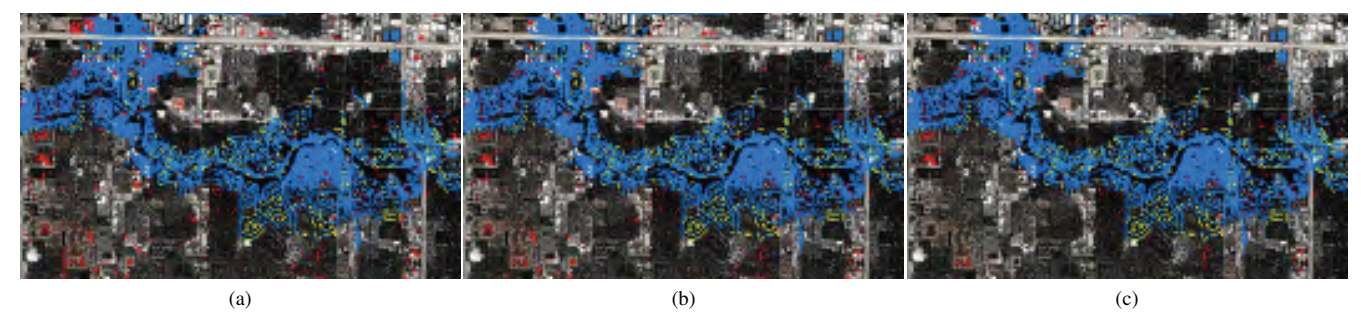


Fig. 8. Harvey: patch direction change based flood mapping with TPs in blue, FPs in red, and FNs in yellow. (a) initial flood map (b) intermediate flood map after spectral filtering, (c) final flood map after spatial filtering.

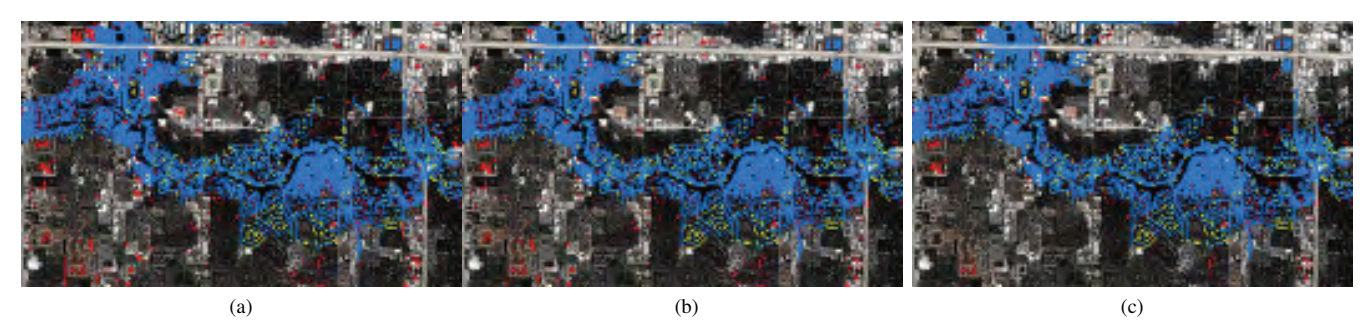


Fig. 9. Harvey: patch magnitude change based flood mapping with TPs in blue, FPs in red, and FNs in yellow. (a) initial flood map (b) intermediate flood map after spectral filtering, (c) final flood map after spatial filtering.

TABLE V
EVALUATION USING DIFFERENT THRESHOLDING METHODS ON THE
direction CHANGE MAP.

Thresholding	Pr	Re	FI	IoU	OA
Rosin [46]	0.8939	0.9175	0.9055	0.8274 0.2894 0.6128	0.9659
Otsu [38]	0.9969	0.2897	0.4489		0.8735
KI [35]	0.6154	0.9934	0.7599		0.8884

maps. After removing building pixels with building footprints, some of initial changed patches were further classified as NF patches, in which no floodwater pixels were found based on the results of the two-class K-Means clustering. Fig. 8b and 9b showed the refined flood maps associated with *direction* and *magnitude* changes, where patches were marked in different colors indicating TPs, FPs, and FNs.

To check how spectral filtering improves the accuracy of patch-wise flood mapping, we also evaluated the associated $Pr,\ Re,\ F1,\ IoU,$ and OA as listed in Table IV.

3) Results of spatial filtering: Results in Figs. 8b and 9b from Section V-A2 after spectral filtering show that there are still small isolated regions of false positive patches marked in red. Constrained by the spatial topology of floodwaters, flooded patches should be close to each other within a flooded region. We also assumed that a flooded region should surpass some minimum area. In this experiment, we tested multiple options of both the maximum distance d for FL patch connectivity and the minimum area a for a flooded region. Figs. 8c and 9c show the final patch-wise flood maps after spatial filtering with d=5 and a=20. Fig. 10 demonstrates the

impact of the hyperparameter a and d on the final patch-wise flood map in terms of the F1 score and IoU based on the direction change. The corresponding quantitative results are summarized in Table IV for both the direction and magnitude change maps at different processing stages.

B. Flood Event 2: Florence

- 1) Results of Patch-CVA: We trained a new patch encoder using the same model architecture (Fig. 3b) with Florence data, which enables better patch feature extraction for the new study area. Following the same processing chain for Harvey data, we obtained two patch-wise flood maps corresponding to the direction (Fig. 11a) and magnitude (Fig. 11c) change maps, respectively. To obtain the initial flood maps, thresholds were selected based on the histograms of the direction (Fig. 11b) and the magnitude (Fig. 11d) change maps using Rosin's method [45], [46]. Figs. 12a and 13a showed the initial flood maps. Corresponding quantitative evaluation is listed in Table. VI.
- 2) Results of spectral filtering: The two-class unsupervised K-Means clustering was performed with all pixels from the potential FL patches detected in Figs. 12a and 13a, respectively. Figs. 12b and 13b show the refined patch-wise flood maps after removing non-flood related patches which were originally classified as FL in the *initial* flood maps (Figs. 12a and 13a) by Patch-CVA. Table VI summarizes the evaluation results associated with the refined *intermediate* flood maps.
- 3) Results of spatial filtering: After removing non-flooded changed patches with spectral filtering, spatial filtering based on spatial topology of floodwaters was applied to further

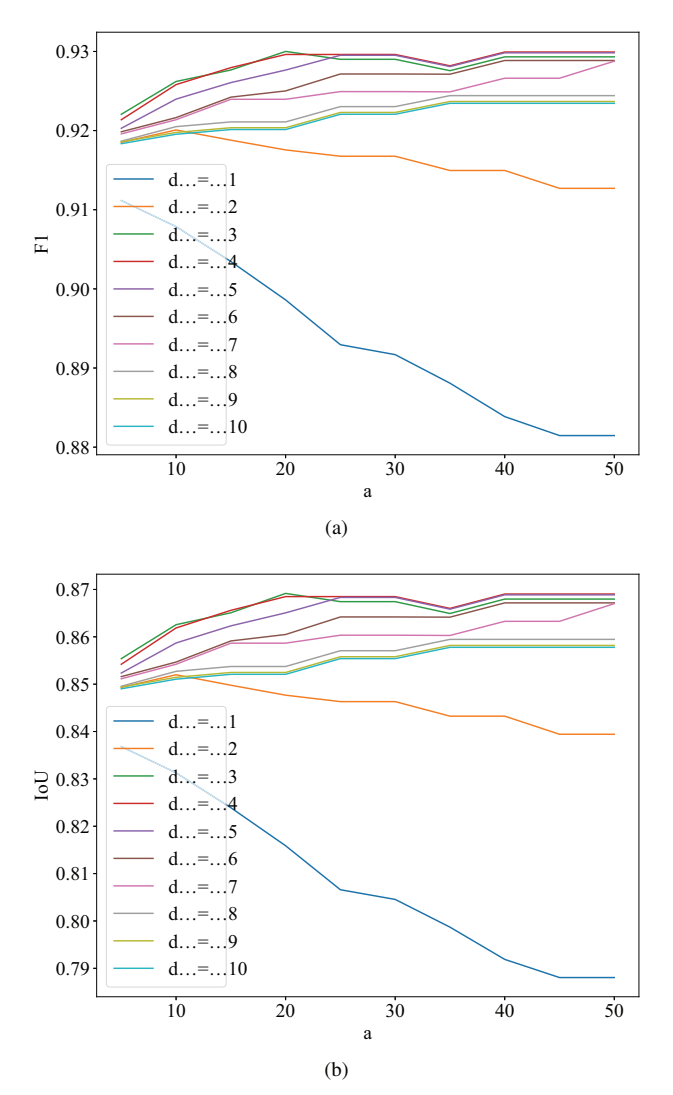


Fig. 10. Harvey: impact of d and a on the (a) F1 and (b) IoU of final flood maps.

TABLE VI FLORENCE: QUANTITATIVE RESULTS OF THE PATCH-WISE FLOOD MAPS AT DIFFERENT PROCESSING STAGES BASED ON THE CHANGE OF direction and magnitude (DIR: DIRECTION; MAG: MAGNITUDE; INT: INITIAL; IMD: INTERMEDIATE; FNL: FINAL)

Type	Stage	Pr	Re	F1	IoU	OA
DIR	(a) INT	0.7355	0.9293	0.8211	0.6965	0.9224
	(b) IMD	0.8249	0.9265	0.8728	0.7743	0.9483
	(c) FNL	0.8352	0.9251	0.8779	0.7823	0.9507
MAG	(a) INT	0.7360	0.9354	0.8238	0.7004	0.9233
	(b) IME	0.8252	0.9326	0.8756	0.7788	0.9492
	(c) FNL	0.8355	0.9311	0.8807	0.7868	0.9517

remove false positive FL patches in the *intermediate* flood maps. We used the same hyperparameters as those in Harvey experiment. Figs. 12c and 13c demonstrated the results of the *final* patch-wise flood maps after spatial filtering.

Associated with Figs. 12c and 13c were the evaluation of Pr, Re, F1, IoU, and OA summarized in Table VI for both the *direction* (Fig. 12c) and *magnitude* (Fig. 13c) change maps.

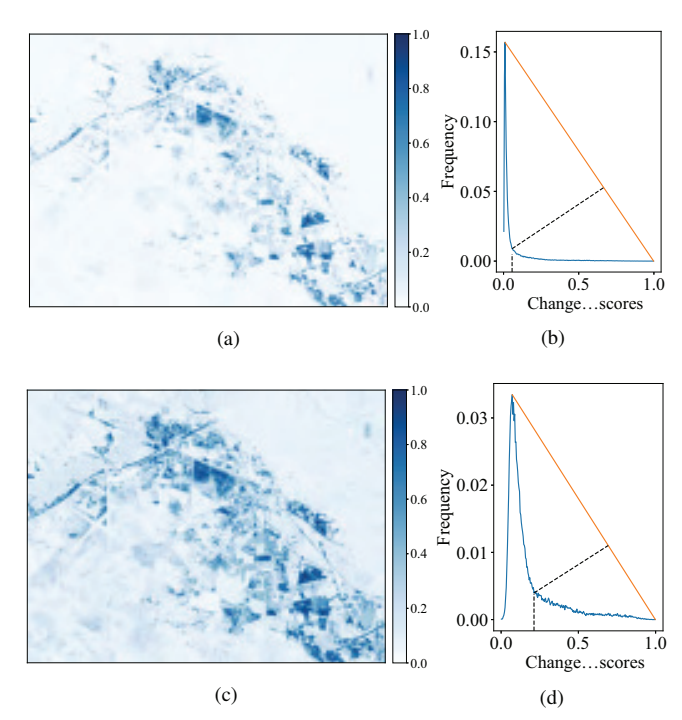


Fig. 11. Florence change maps based on encoded pre- and post-flood patch features: (a) *direction* change map and (b) histogram with Rosin's thresholding corresponding to *direction* change; (c) *magnitude* change map and (d) histogram with Rosin's thresholding corresponding to *magnitude* change.

We also experimented with different (d,a) to show their impact on the accuracy of the final patch-wise flood extent maps. Fig. 14 plotted the change of F1 and IoU with respect to various (d,a).

VI. DISCUSSION

A. Patch Feature Learning

The proposed method starts with patch feature extraction by a patch encoder trained with the input data without manual feature engineering. Such a self-supervised learning framework enables automatic learning of patch features and generalized well to both study areas because the model was trained with local data. This feature is critical for near realtime automated flood mapping since traditional hand-crafted features often fail to generalize well to new data sets associated with heterogeneous image background, which is common in urban areas. Without patch feature extraction, patch-wise flood mapping cannot be implemented through direct pixel-wise processing.

To demonstrate the power of patch features learned by the proposed method, we tested (1) the raw pixel feature and (2) the patch feature extracted by principal component analysis (PCA) for patch-wise flood mapping. First, we computed the pixel-wise magnitude change between the pre- and post-flood images (\mathbf{I}^{pre} , \mathbf{I}^{post}) and obtained the patch-wise magnitude change map via aggregation of pixel-wise magnitude change across each patch. Second, PCA was used to extract features from each pair of pre- and post-flood patches and we kept the first two principal components for further patch-wise

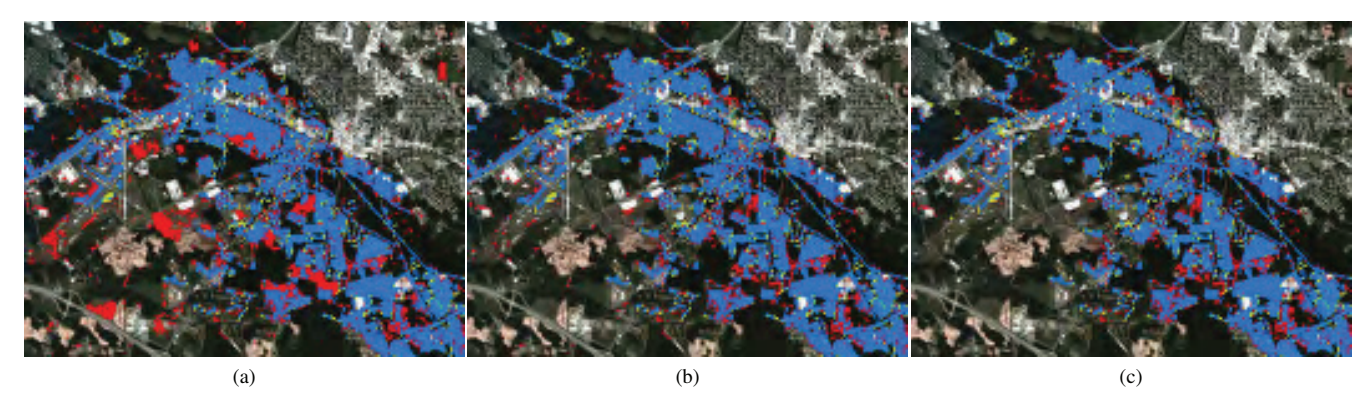


Fig. 12. Florence: patch direction change based flood mapping with TPs in blue, FPs in red, and FNs in yellow. (a) initial flood map (b) intermediate flood map after spectral filtering, (c) final flood map after spatial filtering.

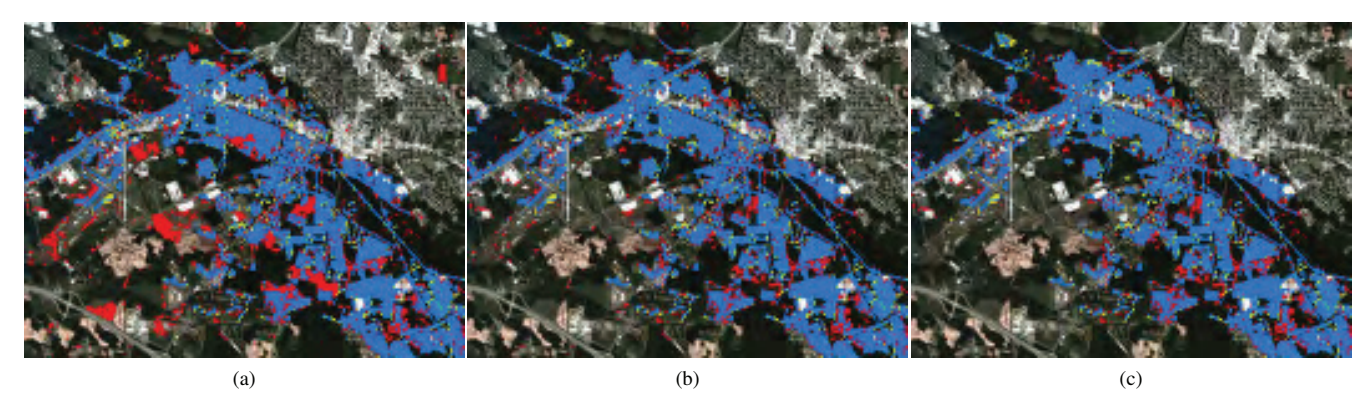


Fig. 13. Florence: patch magnitude change based flood mapping with TPs in blue, FPs in red, and FNs in yellow. (a) initial flood map (b) intermediate flood map after spectral filtering, (c) final flood map after spatial filtering.

TABLE VII

HARVEY: EVALUATION OF THE *initial magnitude* CHANGE MAPS BY ESTIMATING PATCH CHANGES WITH DIFFERENT METHODS: (1) AGGREGATION OF RAW PIXEL FEATURE CHANGE, (2) COMPUTING CHANGE OF PATCH FEATURES EXTRACTED BY PCA, AND (3) COMPUTING CHANGE OF PATCH FEATURES LEARNED BY THE AUTOENCODER EMPLOYED IN THE PROPOSED FRAMEWORK.

Change Map	Pr	Re	F1	IoU	OA
Raw pixel PCA	0.8524 0.3745	0.7717 0.1149	0.8100 0.1759	0.6807 0.0964	0.9356 0.8084
Autoencoder	0.8579	0.9313	0.8931	0.8068	0.9603

flood mapping. Table VII summarizes the results of patchwise *initial* flood mapping for Hurricane Harvey based on the raw pixel feature and the PCA extracted feature without further spectral and spatial filtering, compared to the results generated by the proposed method (i.e., Patch-CVA with *magnitude* change). Rosin's method was used for thresholding both change maps. The results show that flood mapping based on the raw pixel feature and the PCA extracted feature fails to capture some of the weak changes resulting from flooding as demonstrated by a lower *Re* than that corresponding to patch feature based processing. It is worth noting that the autoencoder employed in the proposed framework significantly outperforms PCA in terms of patch feature learning for patch-

wise flood mapping.

Similarly, we performed flood mapping based on raw pixel feature change for Hurricane Florence. Fig. 15a shows that direct pixel-wise change estimation leads to a large number of false positives due to non-informative changes such as varying illumination, inaccurate radiometric correction, and poor image registration. The corresponding histogram (Fig. 15b) also exhibits completely different patterns than those associated with patch-wise change maps, leading to the failure of Rosin's, Otsu's, or KI's thresholding techniques.

B. Comparison of Direction and Magnitude Change

As shown in the experimental results for both Harvey and Florence floods, there is no significant difference between direction and magnitude change-based patch-wise flood mapping, as demonstrated by 1) quantitative evaluation of Pr, Re, F1, IoU, and OA in Table IV for Harvey and Table VI for Florence, and 2) by qualitative visual inspection of the final patch-wise flood maps in Fig. 9c for Harvey and Fig. 13c for Florence.

However, we observed in Figs. 7 and 11 that the *direction* change map showed more abrupt change around the selected threshold while the *magnitude* change map changed more gradually, which was also reflected by the respective histograms. The abrupt change around the threshold indicated

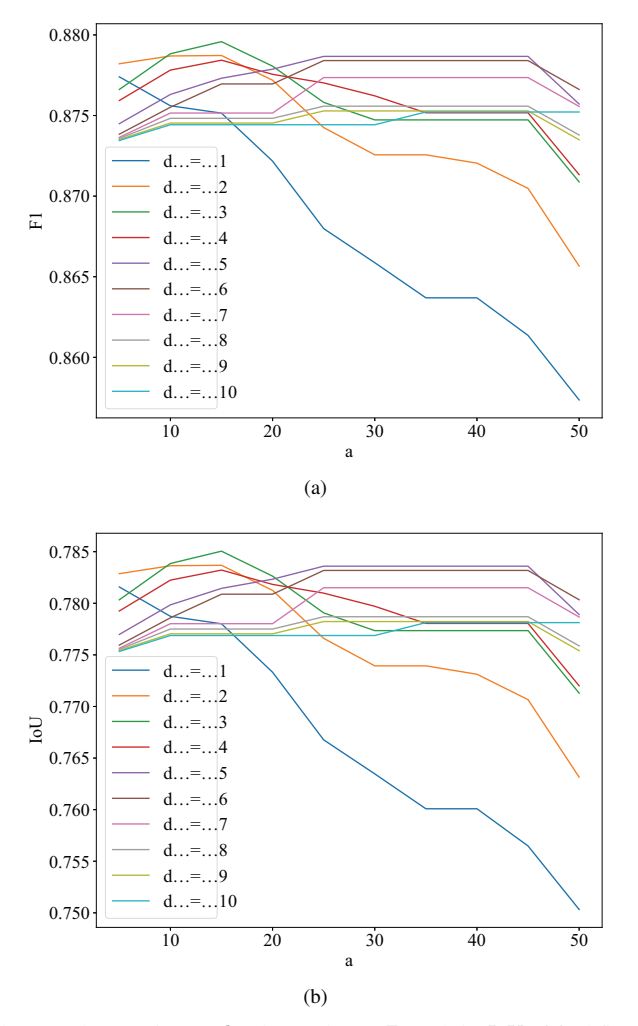


Fig. 14. Florence: impact d and a on the (a) F1 and (b) IoU of final flood extent maps.

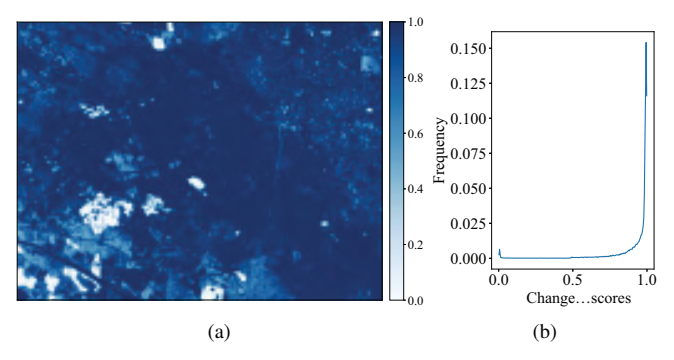
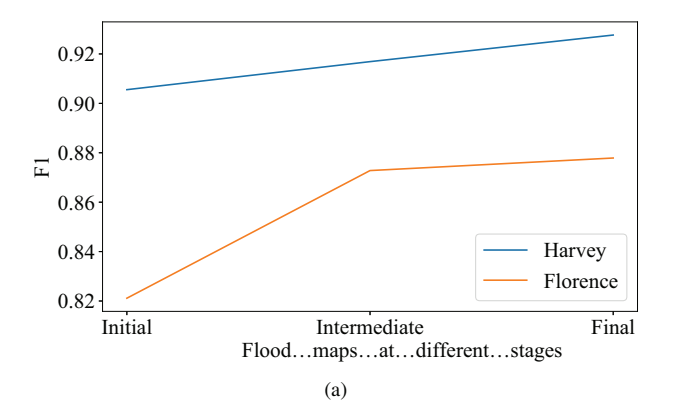


Fig. 15. Florence: (a) *initial* change map based on aggregation of pixel-wise *magnitude* change across each patch, and (b) the corresponding histogram.

that the patch *direction* change-based processing encouraged separation of FL from NF patches with higher contrast compared to *magnitude*-based change estimation.

Furthermore, as *direction* change is more invariant to changes in illumination compared to *magnitude* change, *direction*-based change detection has the potential to suppress minor non-informative changes due to varying illumination, as demonstrated in Figs. 7a and 11a, in which salient changes



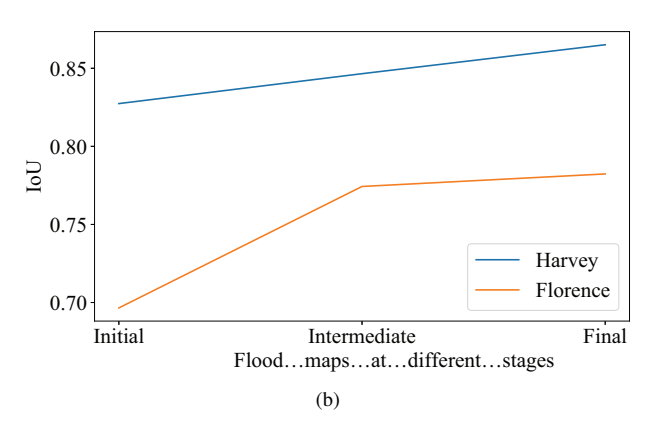


Fig. 16. Impact of spectral and spatial filtering on the (a) F1 and (b) IoU of flood extent maps.

were highlighted whereas subtle changes were suppressed.

C. Impact of Spectral and Spatial Filtering

To demonstrate how spectral and spatial filtering have refined the patch-wise flood maps, Figs. 8 and 12 present the patch *direction* change-based flood maps sequentially for visual inspection of Harvey and Florence floods with corresponding quantitative evaluation illustrated in Fig. 16, where *Initial*, *Intermediate*, *Final* correspond to the results of the *initial* flood maps based on Patch-CVA (Fig. 8a), the *intermediate* flood maps after spectral filtering (Fig. 8b), and the *final* flood maps after spatial filtering (Fig. 8c).

It is obvious that the sequential processing through spectral and spatial filtering improve accuracy in terms of F1 and IoU based on the initial patch-wise flood maps. Spectral filtering helped remove non-floodwater related changes. With a two-class K-Means clustering of all pixels from the initial changed patches, most non-flooded patches were removed. Spatial filtering considered noise and incorrect classification of a few false positive patches from previous steps. In particular, a few small isolated changed patches remained after Patch-CVA and spectral filtering. Those small regions were further removed by leveraging the spatial topology of the flooded regions. In this study, flooded patches were constrained to be close to each other with distance less than 5 patches in a major flooded region with area of at least 20 patches. Final flood maps for both Harvey and Florence floods highlight the robust performance of the proposed method.

Regarding the spatial filtering hyperparameters, (d, a), Fig. 10 shows the impact of different (d, a) on the accuracy of the final flood maps in terms of F1 and IoU based on the direction change. We noted that the performance dropped significantly if we constrained the maximum distance of FL patch connectivity strictly with d = 1. That is, FL patches were connected only if they were strictly adjacent to their neighborhoods. There are several contributing explanations. Some FL patches under tree canopy are labeled as NF patches [12], [21]; such conditions are common in urban areas. As a result, ground truth flood maps may contain FL patches that are disconnected with the neighboring flooded regions. In addition, false negative patches could result from thresholding of the initial flood maps, spectral filtering for the intermediate flood maps, and image noise. As such, we assumed that any two FL patches were connected if they were within a maximum distance of d patches. The other hyperparameter aalso influences the performance of spatial filtering for final flood mapping. We observed that, in ground truth flood maps, some flooding occurred in localized flooded areas relatively far from other flooded patches. Though the localized flooded regions are isolated relative to the major flooded regions, however, they should have some area greater than a pre-defined empirical value a. As some small FL patches are attributable noise or other errors (e.g., small area of the wet road surface), and not removed before spatial filtering, such an assumption contributed to further refinement of the final flood maps.

In this study, spectral filtering and spatial filtering are two interlocking sequential modules for producing the final flood maps. Hence, spectral filtering is a prerequisite for spatial filtering to ensure the robustness and effectiveness of spatial filtering. To further prove the effectiveness of spatial filtering, we conducted spatial filtering alone based on the initial direction change-based flood maps without spectral filtering. Table VIII shows that the F1 and IoU of flood maps after only spatial filtering are higher than those of the initial flood maps, demonstrating the effectiveness of spatial filtering without spectral filtering. However, comparing the results with only spatial filtering to those with the sequential (spectral filtering + spatial filtering), we observe that spectral filtering plays a key role as the prerequisite for spatial filtering. Spatial filtering is used based on the spatial topology of floods (i.e., small isolated and changed areas are considered as nonflooded). Without spectral filtering, there remain some large non-flooded but changed areas connected with major flooded areas, resulting in less effective spatial filtering to filter out such false positive changes. With spectral filtering performed before spatial filtering, most of the large non-flooded but changed areas are removed. Then the remaining non-flooded but changed areas are smaller and isolated from major flooded areas such that spatial filtering performs better for producing the final flood maps. Therefore, it is important to perform spectral filtering and spatial filtering sequentially to ensure the accuracy of the final flood maps.

D. Model Performance across Different Study Areas

Fig. 16 shows that the model performs well for urban flood mapping, with F1 above 0.87 and IoU above 0.78,

TABLE VIII

EVALUATION OF F1 AND IoU FOR FLOOD MAPS AFTER THE SEQUENTIAL (SPECTRAL FILTERING + SPATIAL FILTERING) AND AFTER ONLY SPATIAL FILTERING BASED ON THE *initial direction* CHANGE-BASED FLOOD MAPS PRODUCED BY PATCH-CVA

Flood	Metric	Initial	Intermediate	Final
	<i>F</i> 1	0.9055	0.9169 (spectral)	0.9276 (spatial)
Harvey		0.7022	0.9205 (only spatial	al)
		0.8274	0.8465 (spectral)	0.8651 (spatial)
	100	0.0271	0.8528 (only spatial	al)
	<i>F</i> 1	0.8211	0.8728 (spectral)	0.8779 (spatial)
Florence	1 1	0.0211	0.8267 (only spatis	al)
		0.6965	0.7743 (spectral)	0.7823 (spatial)
	100	0.0703	0.7047 (only spatial	al)

highlighting the model's capability in near realtime processing for upcoming unseen floods.

The evaluations of F1 and IoU associated with the Florence flood were lower than those with the Harvey flood. These differences were due mainly to different degrees of non-flooded changes between the bi-temporal data corresponding to the Harvey and Florence floods over different study areas, respectively. As demonstrated in Figs. 12a and 13a for Florence, the initial flood maps exhibit higher rates of FPs (i.e., non-flooded changes marked in red) than those corresponding to the initial flood maps (Figs. 8a and 9a) for Harvey.

With spectral and spatial filtering, the majority of the FPs were removed as demonstrated by the increasing Pr in Table IV and VI. The Florence *final* flood maps contain a higher rate of FPs compared to the Harvey *final* flood maps. Potential causes include: (1) many FPs in the Florence *final* flood maps consist of pixels with spectra similar to those of floodwaters such as patches that are wet but not flooded, leading to misclassification in spectral filtering; and (2) quite a few FPs in the Florence *final* flood maps are mixed and connected with TPs, which were not removed by spatial filtering. As a result, there remain higher rates of FPs in both *direction* and *magnitude* change-based *final* flood maps in the Florence experiment.

As the main goal of this study is to map urban floods in near realtime, time consumption on training and testing the models plays an important role. Deep learning based models are often time-consuming due to the training of deep neural networks with a large volume of data. Table III shows that it took 40.97 mins and 46.76 mins for training the autoencoders corresponding to the Harvey and Florence floods, respectively. Additionally, it took less than 1 min to encode all pre- and post-flood image patches into patch features. Such features were then used for further Patch-CVA, spectral filtering, and spatial filtering, which also took negligible time to produce the final flood maps. Hence, the total time consumption of the proposed self-supervised learning framework was less than 1 hour for mapping floods at two different urban areas with bitemporal satellite multispectral images, enabling near realtime processing for emergency response.

E. Comparison of Different Thresholding Methods

Automatic thresholding of the *initial direction* or *magnitude* change maps is critical for identifying *initial* flooded patches for further spectral and spatial filtering. As demonstrated by Figs. 7 and 11, the histograms exhibit unimodal distributions for both *direction* and *magnitude* change maps associated with Harvey and Florence data. Table V shows that Rosin's *corner*-based thresholding method achieved superior performance without specific assumption of the foreground or background sample distribution. Note that the foreground samples consisted of changed post-flood patches, while the background samples were unchanged ones.

It is worth noting that Otsu's thresholding method tends to set a larger threshold than the one by Rosin's method, as demonstrated by the low recall Re but high precision Pr of the *initial* flood maps. One assumption of Otsu's method is that the histogram of the image is a bimodal distribution. Additionally, Otsu's method achieves good performance when the valley between the two peaks of the histogram is deep and sharp [51]. As shown in Figs. 7 and 11, however, the histograms of both *direction* and *magnitude* change maps for Harvey and Florence data exhibit unimodal distributions with only one major peak.

In contrast, KI's minimum error thresholding method picked up a smaller threshold compared to Rosin's threshold, leading to a low precision Pr but a high recall Re. The minimum error thresholding method assumes that foreground and background samples are both normally distributed with distinct mean and standard deviations [35]. This assumption was not true in either *direction* or *magnitude* change maps. Neither FL nor NF patches exhibit a normal distribution in the histogram of either *direction* or *magnitude* change maps.

VII. CONCLUSIONS

We propose a fully-automated patch-wise urban flood extent mapping method via a self-supervised learning framework. The before- and after-flood patch features were automatically learned through a self-supervised autoencoder. Patch change vector analysis (Patch-CVA) was performed based on patch features learned from the pre-trained encoder of the autoencoder model, which generated the patch-wise direction and magnitude change maps. Potential flooded patches were extracted through robust binarization of the corresponding change maps, where the binarization thresholds were picked at the change intensity corresponding to the corners of the unimodal change map histograms. Since noise and other errors can cause false alarms in flood mapping, spectral and spatial filtering were performed on the initial patch-wise flood maps by leveraging the spectral signatures and spatial topology of floodwaters. Our results show that the proposed method achieves good performance for both Harvey and Florence floods in terms of F1, IoU, and OA. For example, we obtained the final flood maps with 0.9276 F1 and 0.8651 IoU for Harvey flood, and 0.8779 F1 and 0.7823 IoU for Florence flood based on respective direction change maps. The self-supervised learning framework enables patch feature learning without a large number of human-annotated training

data. The pre-trained patch encoder extracts informative features from both pre- and post-flood patches, where no hand-crafted feature engineering is required. The majority of the desired changes were detected through Patch-CVA based on the corresponding patch features as demonstrated by the *initial* flood maps. Spectral and spatial filtering further boosts the performance by removing non-flood related changes and noise.

Regarding the future work on near realtime flood mapping in practice, optical MS imagery may not be available due to the impact of clouds. It is likely worth testing the proposed method using SAR data or a fusion of SAR and optical data, to take advantage of the nighttime and all-weather data acquisition capability of SAR. Moreover, when only limited number of human annotated training data are available, we would like to try semi-supervised learning, transfer learning, and active learning for further improvement of flood mapping accuracy over heterogeneous urban areas.

REFERENCES

- [1] USGS, "Flood Inundation Mapping (FIM) Program," 2019. [Online]. Available: https://www.usgs.gov/mission-areas/water-resources/science/flood-inundation-mapping-fim-program?qt-science_center_objects=0#qt-science_center_objects
- [2] P. J. Pilon, "Guidelines for reducing flood losses," United Nations International Strategy for Disaster Reduction (UNISDR), Tech. Rep., 2002.
- [3] United Nations, "The Sustainable Development Goals Report," 2018.[Online]. Available: https://www.un.org/sustainabledevelopment/cities
- [4] L. Li, Y. Chen, X. Yu, R. Liu, and C. Huang, "Sub-pixel flood inundation mapping from multispectral remotely sensed images based on discrete particle swarm optimization," *ISPRS Journal of Photogrammetry and Remote Sensing*, vol. 101, pp. 10–21, mar 2015.
- [5] R. Malinowski, G. Groom, W. Schwanghart, and G. Heckrath, "Detection and delineation of localized flooding from WorldView-2 multispectral data," *Remote sensing*, vol. 7, no. 11, pp. 14853–14875, 2015.
- [6] P. Wang, G. Zhang, and H. Leung, "Improving super-resolution flood inundation mapping for multispectral remote sensing image by supplying more spectral information," *IEEE Geoscience and Remote Sensing Letters*, 2018.
- [7] M. Wieland and S. Martinis, "A Modular Processing Chain for Automated Flood Monitoring from Multi-Spectral Satellite Data," *Remote Sensing*, vol. 11, no. 19, p. 2330, oct 2019. [Online]. Available: https://www.mdpi.com/2072-4292/11/19/2330
- [8] L. Zhang, B. Peng, F. Zhang, L. Wang, H. Zhang, P. Zhang, and Q. Tong, "Fast Real-Time Causal Linewise Progressive Hyperspectral Anomaly Detection via Cholesky Decomposition," *IEEE Journal of Selected Topics in Applied Earth Observations and Remote Sensing*, vol. 10, no. 10, pp. 4614–4629, oct 2017. [Online]. Available: http://ieeexplore.ieee.org/document/7994668/
- [9] B. Peng, L. Zhang, T. Wu, and H. Zhang, "Fast real-time target detection via target-oriented band selection," in 2016 IEEE International Geoscience and Remote Sensing Symposium (IGARSS). IEEE, jul 2016, pp. 5868–5871. [Online]. Available: http://ieeexplore.ieee.org/document/7730533/
- [10] B. Du, Q. Wei, and R. Liu, "An Improved Quantum-Behaved Particle Swarm Optimization for Endmember Extraction," *IEEE Transactions on Geoscience and Remote Sensing*, vol. 57, no. 8, pp. 6003–6017, aug 2019. [Online]. Available: https://ieeexplore.ieee.org/document/8681118/
- [11] L. Tong, B. Du, R. Liu, and L. Zhang, "An Improved Multiobjective Discrete Particle Swarm Optimization for Hyperspectral Endmember Extraction," *IEEE Transactions on Geoscience and Remote Sensing*, vol. 57, no. 10, pp. 7872–7882, oct 2019. [Online]. Available: https://ieeexplore.ieee.org/document/8734750/
- [12] B. Peng, Z. Meng, Q. Huang, and C. Wang, "Patch Similarity Convolutional Neural Network for Urban Flood Extent Mapping Using Bi-Temporal Satellite Multispectral Imagery," *Remote Sensing*, vol. 11, no. 21, p. 2492, oct 2019. [Online]. Available: https://www.mdpi.com/2072-4292/11/21/2492

- [13] B. Peng, X. Liu, Z. Meng, and Q. Huang, "Urban Flood Mapping with Residual Patch Similarity Learning," in *Proceedings* of the 3rd ACM SIGSPATIAL International Workshop on AI for Geographic Knowledge Discovery - GeoAI 2019. New York, New York, USA: ACM Press, 2019, pp. 40–47. [Online]. Available: http://dl.acm.org/citation.cfm?doid=3356471.3365235
- [14] Planet Team, "Planet Application Program Interface: In Space for Life on Earth. San Francisco, CA." 2018. [Online]. Available: https://api.planet.com
- [15] DigitalGlobe, "Open Data Program." [Online]. Available: https://www.digitalglobe.com/ecosystem/open-data
- [16] M. Xie, Z. Jiang, and A. M. Sainju, "Geographical hidden markov tree for flood extent mapping," in *Proceedings of the 24th ACM SIGKDD International Conference on Knowledge Discovery & Data Mining*, 2018, pp. 2545–2554.
- [17] S. Skakun, "A neural network approach to flood mapping using satellite imagery," *Computing and Informatics*, vol. 29, no. 6, pp. 1013–1024, 2012.
- [18] P. Insom, C. Cao, P. Boonsrimuang, D. Liu, A. Saokarn, P. Yomwan, and Y. Xu, "A support vector machine-based particle filter method for improved flooding classification," *IEEE Geoscience and Remote Sensing Letters*, vol. 12, no. 9, pp. 1943–1947, 2015.
- [19] Q. Feng, J. Liu, and J. Gong, "Urban Flood Mapping Based on Unmanned Aerial Vehicle Remote Sensing and Random Forest Classifier A Case of Yuyao, China," Water, vol. 7, no. 12, pp. 1437–1455, mar 2015.
- [20] A. Gebrehiwot, L. Hashemi-Beni, G. Thompson, P. Kordjamshidi, and T. Langan, "Deep Convolutional Neural Network for Flood Extent Mapping Using Unmanned Aerial Vehicles Data," *Sensors*, vol. 19, no. 7, p. 1486, mar 2019.
- [21] Y. Li, S. Martinis, and M. Wieland, "Urban flood mapping with an active self-learning convolutional neural network based on TerraSAR-X intensity and interferometric coherence," ISPRS Journal of Photogrammetry and Remote Sensing, vol. 152, pp. 178–191, jun 2019. [Online]. Available: https://linkinghub.elsevier.com/retrieve/pii/S092427161930111X
- [22] T. Liu, L. Yang, and D. D. Lunga, "Towards Misregistration-Tolerant Change Detection using Deep Learning Techniques with Object-Based Image Analysis," in *Proceedings of the 27th ACM SIGSPATIAL International Conference on Advances in Geographic Information Systems SIGSPATIAL 19.* New York, New York, USA: ACM Press, 2019, pp. 420–423. [Online]. Available: http://dl.acm.org/citation.cfm?doid=3347146.3359068
- [23] L. Bruzzone and R. Cossu, "An adaptive approach to reducing registration noise effects in unsupervised change detection," *IEEE Transactions on Geoscience and Remote Sensing*, vol. 41, no. 11, pp. 2455–2465, nov 2003. [Online]. Available: http://ieeexplore.ieee.org/document/1245234/
- [24] Y. Byun, Y. Han, and T. Chae, "Image Fusion-Based Change Detection for Flood Extent Extraction Using Bi-Temporal Very High-Resolution Satellite Images," *Remote Sensing*, vol. 7, no. 8, pp. 10347–10363, aug 2015. [Online]. Available: http://www.mdpi.com/2072-4292/7/8/10347
- [25] FEMA, "Federal Emergency Management Agency Flood Mapping Products." [Online]. Available: https://www.fema.gov/flood-mappingproducts
- [26] L. Jing and Y. Tian, "Self-supervised Visual Feature Learning with Deep Neural Networks: A Survey," *IEEE Transactions on Pattern Analysis and Machine Intelligence*, pp. 1–1, 2020. [Online]. Available: https://ieeexplore.ieee.org/document/9086055/
- [27] A. Kolesnikov, X. Zhai, and L. Beyer, "Revisiting Self-Supervised Visual Representation Learning," in *Proceedings of the IEEE Conference* on Computer Vision and Pattern Recognition, jan 2019, pp. 1920–1929. [Online]. Available: http://arxiv.org/abs/1901.09005
- [28] I. Goodfellow, Y. Bengio, and A. Courville, *Deep learning*. MIT press, 2016.
- [29] H. Song, Y. Kim, and Y. Kim, "A Patch-Based Light Convolutional Neural Network for Land-Cover Mapping Using Landsat-8 Images," *Remote Sensing*, vol. 11, no. 2, p. 114, 2019.
- [30] A. Sharma, X. Liu, X. Yang, and D. Shi, "A patch-based convolutional neural network for remote sensing image classification," *Neural Net*works, vol. 95, pp. 19–28, 2017.
- [31] A. S. Dhakal, T. AMADA, M. ANIYA, and R. R. SHARMA, "Detection of areas associated with flood and erosion caused by a heavy rainfall using multitemporal landsat tm data," *Photogrammetric engineering and* remote sensing, vol. 68, no. 3, pp. 233–239, 2002.
- [32] S. Schlaffer, P. Matgen, M. Hollaus, and W. Wagner, "Flood detection from multi-temporal SAR data using harmonic analysis and change

- detection," *International Journal of Applied Earth Observation and Geoinformation*, vol. 38, pp. 15–24, jun 2015. [Online]. Available: https://linkinghub.elsevier.com/retrieve/pii/S0303243414002645
- [33] L. Giustarini, R. Hostache, P. Matgen, G. J.-P. Schumann, P. D. Bates, and D. C. Mason, "A Change Detection Approach to Flood Mapping in Urban Areas Using TerraSAR-X," *IEEE Transactions on Geoscience and Remote Sensing*, vol. 51, no. 4, pp. 2417–2430, apr 2013. [Online]. Available: http://ieeexplore.ieee.org/document/6297453/
- [34] N. Longbotham, F. Pacifici, T. Glenn, A. Zare, M. Volpi, D. Tuia, E. Christophe, J. Michel, J. Inglada, J. Chanussot, and Q. Du, "Multi-Modal Change Detection, Application to the Detection of Flooded Areas: Outcome of the 2009–2010 Data Fusion Contest," *IEEE Journal of Selected Topics in Applied Earth Observations and Remote Sensing*, vol. 5, no. 1, pp. 331–342, feb 2012. [Online]. Available: http://ieeexplore.ieee.org/document/6144016/
- [35] J. Kittler and J. Illingworth, "Minimum error thresholding," *Pattern recognition*, vol. 19, no. 1, pp. 41–47, 1986. [Online]. Available: https://linkinghub.elsevier.com/retrieve/pii/0031320386900300
- [36] G. Moser and S. Serpico, "Generalized minimum-error thresholding for unsupervised change detection from SAR amplitude imagery," *IEEE Transactions on Geoscience and Remote Sensing*, vol. 44, no. 10, pp. 2972–2982, oct 2006. [Online]. Available: http://ieeexplore.ieee.org/document/1704990/
- [37] F. Greifeneder, W. Wagner, D. Sabel, and V. Naeimi, "Suitability of SAR imagery for automatic flood mapping in the Lower Mekong Basin," *International Journal of Remote Sensing*, vol. 35, no. 8, pp. 2857–2874, apr 2014. [Online]. Available: https://www.tandfonline.com/doi/full/10.1080/01431161.2014.890299
- [38] N. Otsu, "A threshold selection method from gray-level histograms," *IEEE transactions on systems, man, and cybernetics*, vol. 9, no. 1, pp. 62–66, 1979. [Online]. Available: http://ieeexplore.ieee.org/document/4310076/
- [39] B. Du, L. Ru, C. Wu, and L. Zhang, "Unsupervised Deep Slow Feature Analysis for Change Detection in Multi-Temporal Remote Sensing Images," *IEEE Transactions on Geoscience and Remote Sensing*, vol. 57, no. 12, pp. 9976–9992, dec 2019. [Online]. Available: https://ieeexplore.ieee.org/document/8824216/
- [40] D. P. Kingma and J. Ba, "Adam: A Method for Stochastic Optimization," in *International Conference for Learning Representations*, may 2015. [Online]. Available: http://arxiv.org/abs/1412.6980
- [41] W. A. Malila, "Change vector analysis: an approach for detecting forest changes with landsat," in *LARS symposia*, 1980, p. 385.
- [42] E. F. Lambin and A. H. Strahlers, "Change-vector analysis in multitemporal space: A tool to detect and categorize land-cover change processes using high temporal-resolution satellite data," *Remote Sensing* of Environment, vol. 48, no. 2, pp. 231–244, may 1994. [Online]. Available: https://linkinghub.elsevier.com/retrieve/pii/0034425794901449
- [43] O. A. Carvalho Júnior, R. F. Guimarães, A. R. Gillespie, N. C. Silva, and R. A. T. Gomes, "A New Approach to Change Vector Analysis Using Distance and Similarity Measures," *Remote Sensing*, vol. 3, no. 11, pp. 2473–2493, nov 2011. [Online]. Available: http://www.mdpi.com/2072-4292/3/11/2473
- [44] S. Saha, F. Bovolo, and L. Bruzzone, "Unsupervised Deep Change Vector Analysis for Multiple-Change Detection in VHR Images," *IEEE Transactions on Geoscience and Remote Sensing*, vol. 57, no. 6, pp. 3677–3693, jun 2019. [Online]. Available: https://ieeexplore.ieee.org/document/8608001/
- Detection," "Thresholding [45] P. Change L. Rosin. for Computer Vision and Image Understanding, vol 86 79_95 2002 may [Online] Available: no. pp. https://linkinghub.elsevier.com/retrieve/pii/S1077314202909604
- [46] P. L. Rosin, "Unimodal thresholding," Pattern Recognition, vol. 34, no. 11, pp. 2083 – 2096, 2001. [Online]. Available: http://www.sciencedirect.com/science/article/pii/S0031320300001369
- [47] D. Amitrano, G. Di Martino, A. Iodice, D. Riccio, and G. Ruello, "Unsupervised Rapid Flood Mapping Using Sentinel-1 GRD SAR Images," *IEEE Transactions on Geoscience and Remote Sensing*, vol. 56, no. 6, pp. 3290–3299, jun 2018. [Online]. Available: https://ieeexplore.ieee.org/document/8291019/
- [48] Microsoft Bing Maps Team, "Microsoft Building Footprints," 2018.
 [Online]. Available: https://www.microsoft.com/en-us/maps/building-footprints
- [49] M. LEVANDOWSKY and D. WINTER, "Distance between Sets," Nature, vol. 234, no. 5323, pp. 34–35, nov 1971. [Online]. Available: http://www.nature.com/articles/234034a0
- [50] P. Adam, G. Sam, C. Soumith, C. Gregory, Y. Edward, D. Zachary, L. Zeming, D. Alban, A. Luca, and L. Adam, "Automatic differentiation

in pytorch," in Proceedings of Neural Information Processing Systems, 2017.

[51] J. Kittler and J. Illingworth, "On threshold selection using clustering criteria," *IEEE Transactions on Systems, Man, and Cybernetics*, no. 5, pp. 652–655, 1985.



Bo Peng is a Ph.D. candidate in Geography (remote sensing track) with a doctoral minor in Electrical Engineering (machine learning track) at University of Wisconsin-Madison. He received the B.E. degree in Remote Sensing Science and Technology from Wuhan University in 2014, the M.S. degree in Cartography and Geographic Information System from University of Chinese Academy of Sciences in 2017, and the M.S. degree in Electrical Engineering from University of Wisconsin-Madison in 2019. His research interests span GeoAI, earth observation,

computer vision, machine learning, and disaster resilience.



Qunying Huang is an associate professor in the Department of Geography at University of Wisconsin-Madison. Her fields of expertise include Spatial Computing, Spatial Data Mining and Spatial Data Analytics. Dr. Huang's research bridges the gap between Computer and Information Science (CI-Science) and GIScience by generating new computational algorithms and methods to make sense of complex big spatial data sets obtained from both the physical (e.g., remote sensing) and social (e.g., social media) sensing networks. The problem domains

of her research are related to natural hazards and human mobility.



Jamp Vongkusolkit is a M.S. student in Geographic Information Science at University of Wisconsin-Madison, where she received the B.S. degree in Environmental Sciences in 2019. She is interested in applying geospatial analysis and spatial modeling to environmental issues and natural disasters. She is also interested in using image processing and analysis techniques on satellite imagery for environmental analyses.



Song Gao is an Assistant Professor in GIScience at the University of Wisconsin-Madison. He holds a Ph.D. degree in Geography at the University of California-Santa Barbara, a M.S. degree in Cartography and GIS at Peking University, and a B.S. degree with Honors at the School of Geography, Beijing Normal University. His main research interests include Place-Based GIS, GeoAI, Geospatial Big Data and Social Sensing.



Daniel B. Wright holds bachelors and masters degrees in Civil and Environmental Engineering from the University of Michigan, and earned his PhD from Princeton University, where he studied urban rainfall and flooding. He worked at the World Bank from 2013-2014, focusing on flood and landslide risk reduction in Latin America and the Caribbean before becoming a NASA Postdoctoral Program fellow at Goddard Space Flight Center from 2014-2016. He joined the Civil and Environmental Engineering Department at UW-Madison as an assistant professor

in 2016. He is a member of NASA's Precipitation Measurement Mission Science Team and received a National Science Foundation CAREER Award in Hydrologic Sciences in 2018. Dr. Wright is a founder and co-chair of the Infrastructure Working Group within the Wisconsin Initiative on Climate Change Impacts, as well as a member of its Science Advisory Board. His research and teaching focuses on floods and how they are influenced by meteorology, urbanization, and climate change.



Zheng N. Fang is an associate professor at the Civil Engineering Department of the University of Texas at Arlington. He received his Ph.D. in Civil and Environmental Engineering from Rice University in 2008. As a Texas licensed PE, Dr. Fang has been actively working on surface water and groundwater problems for over 17 years including floodplain studies, hydrologic/hydraulic modeling, water treatment, hydrodynamic simulation, storm water management modeling, and water quality assessment for a number of watersheds and areas in Texas, Florida, Georgia,

Connecticut, California, and Louisiana. Dr. Fang has been conducting quality research in the areas of inland flood prediction and hurricane-induced storm surge, urban hydraulic prediction tool- FloodPlain Map Library (FPML), advanced radar-based flood warning system, dynamic moving storm (DMS) generator and stochastic storm transposition (SST), climate forecast-aided drought decision support, integrated sensing and prediction of urban water, evaluation of urbanization and infiltration, and Unmanned Aerial Vehicles (UAVs) Enabled Data Collection System for hydrology and hydraulics. Dr. Fang is a contributing member to the state emergency operations during Hurricane Harvey (2017) for the Texas Division of Emergency Management (TDEM), the U.S. Army Corps of Engineers (USACE), the Texas Medical Center (TMC), Rice University, and the U.T. MD Anderson Cancer Center.



Yi Qiang is an assistant professor at the School of Geosciences, University of South Florida. He holds a Ph.D. in Geography from Ghent University, Belgium, M.Sc. in Geographical Information Science from University of Edinburgh, and B.Sc. in Geographic Information Systems from Beijing Normal University. His research focuses on GI-Science, spatial data science and geovisualization. He leads multiple research projects in space-time modeling, GeoAI and data-driven methods for disaster resilience assessment.